Proceedings of the ASME 2010 3rd Joint US-European Fluids Engineering Summer Meeting and 8th International Conference on Nanochannels, Microchannels, and Minichannels
FEDSM-ICNMM2010
August 1-5, 2010, Montreal, Canada

FEDSM-ICNMM2010-31135

BLUFF-BODY SIMULATION BY SPH METHOD WITH RELATIVELY HIGH REYNOLDS NUMBER IN LAMINAR FLOW REGIME

Mostafa Safdari Shadloo
Sabanci University, Faculty of Engineering and Natural Sciences, PhD. Student
Istanbul, Turkey

Amir Zainali
Sabanci University, Faculty of Engineering and Natural Sciences, MSc. Student
Istanbul, Turkey

Mehmet Yildiz
Sabanci University, Faculty of Engineering and Natural Sciences, Faculty Member
Istanbul, Turkey

ABSTRACT

In this work, we present solutions for flow over an airfoil and square obstacle using Weakly Compressible Smoothed Particle Hydrodynamics (WCSPH) method. For the solution of these two problems, we present an improved WCSPH algorithm that can handle complex geometries with the usage of multiple tangent solid boundary method, and eliminate particle clustering induced instabilities with the implementation of particle fracture repair procedure as well as the corrected SPH discretization scheme. We have shown that the improved WCSPH method can be effectively used for flow simulations over bluff-bodies with Reynolds numbers as high as 1400, which is not achievable with standard WCSPH formulations. Our simulation results are validated with a Finite Element mesh-dependent Method (FEM), and excellent agreements among the results were observed. We illustrated that the improved WCSPH method is able to capture the complex physics of bluff-body flows naturally such as flow separation, detachment of separated flow, wake formation at the trailing edge, and vortex shedding without any extra effort to increase the particle resolution in some specific areas of interest.

INTRODUCTION

There are several complex flow phenomena such as separation, circulation and reattachment in many industrial and engineering problems [1, 2]. These phenomena occurs in various practical application like water channels design, heat transfer performance of fins, sudden expansion in air conditioning ducts, flow behaviors in a diffuser, and flow around structures. Square obstacle and airfoil are appropriate geometries for revealing the fundamental characteristics of the fluid flow around structures. In light of this, they became widely modeled benchmark problems to validate new Computational Fluid Dynamic (CFD) approaches as well as to show the capability and the accuracy of developing algorithms.

Smoothed Particles Hydrodynamics (SPH) is one of the most successful meshless computational methods, which was introduced separately by Gingold and Monaghan [3] and Lucy [4] in 1977 to simulate astrophysical problems. Lately, it has attracted significant attention of the fluid and solid mechanics as well computer graphics communities, and in turn has been utilized to solve a wide variety of complex and highly non-linear engineering problems [5-8]. In this method, instead of using Eulerian fixed mesh, the computational domain is represented by a set of particles which are allowed to move in accordance with the solutions of relevant governing and constitutive equations. In fact, the aforementioned particles are merely movable points which carry relevant physical and hydrodynamic transport properties such as temperature, enthalpy, density, viscosity and so forth. The Lagrangian nature of SPH lends itself remarkably to the simulation of a variety of complex fluid flow processes such as flow around bluff-bodies.

One of the common approaches for solving the balance of the linear momentum equation utilized in the SPH literature is the Weakly Compressible SPH (WCSPH), implemented in this work. In this approach, the pressure term in the momentum equation is computed explicitly from a simple thermodynamic equation of state.

It has been reported in the SPH literature that the WCSPH method suffers dramatically when dealing with fluid flow problems characterized by higher Reynolds number values [9, 10]. Therefore in this work, we have suggested and implemented an improved SPH algorithm for the WCSPH approach. The improved algorithm comprises; i-) the MBT method to treat solid boundaries with complex geometries [11], ii-) the artificial particle displacement procedure to repair the

non-uniformity and local fractures in particle distributions as well as iii-) the corrective SPH discretization scheme to circumvent the particle inconsistency problem and in turn enhance the accuracy of overall computation. The WCSPH method is implemented on two bluff body test cases, namely square obstacle and airfoil problems. It is shown that the WCSPH results for both intermediate and higher Reynolds number values in laminar regime are in good agreement with those in FEM methods.

Keywords: Smoothed Particle Hydrodynamics (SPH), Meshless methods, Bluff-body, Airfoil problem, Square obstacle problem

NOMENCLATURE

C_{CFL}	Courant-Friedrichs-Lewy coefficient
F^B	Magnitude of body force vector
$\vec{\mathbf{f}}^B$	Body force vector
H	The height of the computational domain
h	Smoothing length
h_{ij}	Averaged smoothing length
$\mathbf{i}$	Particle identifier for a center particle
$\underline{\underline{\mathbf{I}}}$	Identity tensor
$\mathbf{j}$	Particle identifier for a neighbor particle
L	The length of the computational domain
l_c	Characteristic length for Reynolds number
L_o	Characteristic length for the speed of sound
m	Maximum camber in percentage of the chord
M	Mach number
$m_{\mathbf{i}}$	Mass corresponding to the $\mathbf{i}^{th}$ particle
n_1	Particle movement method constant
n_2	Particle movement method constant
n_i	Number density
P	Pressure
p	Position of the maximum camber in percentage of the chord
P_o	Reference pressure
$\vec{\mathbf{r}}_{\mathbf{i}}$	Position vector
r_{ij}	Magnitude of the distance between the particles $\mathbf{i}$ and $\mathbf{j}$
r_o	Cutoff distance
s_{ij}	Normalized distance with respect to smoothing length
t	Time
$\underline{\underline{\mathbf{T}}}$	Viscous stress tensor
$\vec{\mathbf{v}}$	Velocity vector
v_b	Bulk velocity
v_{max}	Maximum value of the fluid velocity
v^x	Velocity component in x direction
v^y	Velocity component in y direction
W	Kernel function
x	x horizontal coordinate system
y	y vertical coordinate system
α_o	Coefficient for quintic spline kernel
β	Artificial particle displacement coefficient
δ	Dirac-delta function
δ_o	Density variation factor to calculate speed of sound
$\delta \mathbf{r}_i^k$	Artificial particle displacement vector
μ	Dynamic viscosity
ρ	Density
ρ_o	Reference density
$\underline{\underline{\boldsymbol{\sigma}}}$	Total stress tensor
φ	Problem dependent coefficient to calculate speed of sound
Ω	Total bounded volume
ϕ	The angle of attach of airfoil

GOVERNING EQUATIONS

The governing equations used to solve the fluid problems in this article are the mass and linear momentum balance equations which are expressed in the Lagrangian form and given in direct notation as

$$D\rho/Dt = -\rho\nabla\bullet\vec{\mathbf{v}} \tag{1}$$

$$\rho D\vec{\mathbf{v}}/Dt = \nabla\bullet\underline{\underline{\boldsymbol{\sigma}}} + \rho\vec{\mathbf{f}}^B \tag{2}$$

In the present simulations, the fluid is assumed to be incompressible and Newtonian. Hence, the incompressibility condition requires that the divergence of the fluid velocity $\nabla\bullet\vec{\mathbf{v}}=0$ be zero. Here, ρ is the fluid density, $\vec{\mathbf{v}}$ is the divergence-free fluid velocity, $\underline{\underline{\boldsymbol{\sigma}}}$ is the total stress tensor, and $\vec{\mathbf{f}}^B$ is the body force term, respectively. The total stress is defined as $\underline{\underline{\boldsymbol{\sigma}}} = -p\underline{\underline{\mathbf{I}}} + \underline{\underline{\mathbf{T}}}$, where p is the absolute pressure, $\underline{\underline{\mathbf{I}}}$ is the identity tensor, $\underline{\underline{\mathbf{T}}}$ is the viscous part of the total stress tensor. Finally, D/Dt is the material time derivative operator defined as $D/Dt = \partial/\partial t + v_l \partial/\partial x_l$.

SPH FORMULATION

The three-dimensional Dirac-delta function, also refer to as a unit pulse function, is the starting point for the SPH approximation technique. This function satisfies the identity

$$f\left(\vec{\mathbf{r}}_{\mathbf{i}}\right) = \int_{\Omega} f\left(\vec{\mathbf{r}}_{\mathbf{j}}\right)\delta^3\left(r_{\mathbf{ij}}\right) d^3\vec{\mathbf{r}}_{\mathbf{j}} \tag{3}$$

where $d^3\vec{\mathbf{r}}_{\mathbf{j}}$ is a differential volume element and Ω represents the total bounded volume.

The SPH approach assumes that the fields of the particle of interest are affected by that of all other particles within the global domain. The interactions among the particles within the global domain are achieved through a compactly supported, normalized and even weighting function (smoothing kernel

function) $W(r_{ij},h)$ with a smoothing radius κh (cut off distance, localized domain) beyond which the function is zero. Hence, in computations, a given particle interacts with only its nearest neighbors contained in this localized domain. Here, the length h defines the support domain of the particle of interest, κ is a coefficient associated with the particular kernel function, and where r_{ij} is the magnitude of the distance between the particle of interest **i** and its neighboring particles **j**. If the Dirac delta function in Equation (3) is replaced by a kernel function $W(r_{\mathbf{ij}},h)$, the integral estimate or the kernel approximation to an arbitrary function $f(\vec{\mathbf{r}}_{\mathbf{i}})$ can be introduced as

$$f(\vec{\mathbf{r}}_{\mathbf{i}}) \cong \langle f(\vec{\mathbf{r}}_{\mathbf{i}}) \rangle \equiv \int_{\Omega} f(\vec{\mathbf{r}}_{\mathbf{j}}) W(r_{\mathbf{ij}},h)\, d^3\vec{\mathbf{r}}_{\mathbf{j}} \tag{4}$$

where the angle bracket $\langle\ \rangle$ denotes the kernel approximation, and $\vec{\mathbf{r}}_{\mathbf{i}}$ is the position vector defining the center point of the kernel function.

Approximation to the Dirac-delta function by a smoothing kernel function is the origin of the smoothed particle hydrodynamics. The Dirac-delta function can be replaced by a smoothing kernel function provided that the smoothing kernel satisfies several conditions; namely, *i)* normalization condition: the area under the smoothing function must be unity over its support domain, $\int_{\Omega} W(r_{\mathbf{ij}},h) d^3\vec{\mathbf{r}}_{\mathbf{j}} = 1$, *ii)* the Dirac-delta function property: as the smoothing length approaches to zero, the Dirac-delta function should be recovered $\lim_{h\to 0} W(r_{\mathbf{ij}},h) = \delta^3(r_{\mathbf{ij}})$, *iii)* compactness property: which necessitates that the kernel function be zero beyond its compact support domain, $W(r_{\mathbf{ij}},h)=0$ when $r_{\mathbf{ij}}>\kappa h$, and *iv)* the kernel function should be spherically symmetric even function, $W(r_{\mathbf{ij}},h)=W(-r_{\mathbf{ij}},h)$, and be positive within the support domain $W(r_{\mathbf{ij}},h)>0$ when $r_{\mathbf{ij}}<\kappa h$. Finally, the value of the smoothing function should decay with increasing distance away from the center particle.

In this work, we have used a quintic spline kernel function suggested by Morris [12]

$$W(r_{ij},h) = \alpha_o \begin{cases} (3-s_{ij})^5 - 6(2-s_{ij})^5 + 15(1-s_{ij})^5 & \text{if } 0 \le s_{ij} < 1 \\ (3-s_{ij})^5 - 6(2-s_{ij})^5 & \text{if } 1 \le s_{ij} < 2 \\ (3-s_{ij})^5 & \text{if } 2 \le s_{ij} \le 3 \\ 0 & \text{if } s_{ij} \ge 3 \end{cases} \tag{5}$$

Here $\alpha_o = \dfrac{7}{478\pi h^2}$ and $s_{ij}=r_{ij}/h$. The spatial resolution of SPH is affected by the smoothing length. Hence, depending on the problem solved, each particle can be assigned to a different value of smoothing length. However, for a variable smoothing length, it is probable to violate Newton's third law. For example, it might be possible for a particle **j** to exert a force on particle **i**, and not to experience an equal and opposite reaction force from particle **i**. To ensure that Newton's third law is not violated and the pair wise interaction among particles moving close to each other is achieved, the smoothing length is substituted by its average, defined as $h_{\mathbf{ij}}=0.5(h_{\mathbf{i}}+h_{\mathbf{j}})$. The averaged smoothing length ensures that particle **i** is within the influence domain of particle **j** and vice versa.

The SPH approximation for the gradient of an arbitrary function (i.e., scalar, vectorial, or tensorial) can be written through the substitution $f(\vec{\mathbf{r}}_{\mathbf{j}}) \to \partial f(\vec{\mathbf{r}}_{\mathbf{j}})/\partial x_{\mathbf{j}}^k$ in Equation (4) to produce

$$\frac{\partial f(\vec{\mathbf{r}}_{\mathbf{i}})}{\partial x_{\mathbf{i}}^k} \cong \left\langle \frac{\partial f(\vec{\mathbf{r}}_{\mathbf{i}})}{\partial x_{\mathbf{i}}^k} \right\rangle \equiv \int_{\Omega} \frac{\partial f(\vec{\mathbf{r}}_{\mathbf{j}})}{\partial x_{\mathbf{j}}^k} W(r_{\mathbf{ij}},h)\, d^3\vec{\mathbf{r}}_{\mathbf{j}} \tag{6}$$

Upon integrating Equation (6) by parts and using compactness property of the kernel function as well as noting that $\partial W(r_{\mathbf{ij}},h)/\partial x_{\mathbf{i}}^k = -\partial W(r_{\mathbf{ij}},h)/\partial x_{\mathbf{j}}^k$ for a constant smoothing length h, it can be shown that

$$\frac{\partial f(\vec{\mathbf{r}}_{\mathbf{i}})}{\partial x_{\mathbf{i}}^k} \cong \left\langle \frac{\partial f(\vec{\mathbf{r}}_{\mathbf{i}})}{\partial x_{\mathbf{i}}^k} \right\rangle \equiv \int_{\Omega} f(\vec{\mathbf{r}}_{\mathbf{j}}) \frac{\partial W(r_{\mathbf{ij}},h)}{\partial x_{\mathbf{j}}^k} d^3\vec{\mathbf{r}}_{\mathbf{j}} \tag{7}$$

Using a Taylor series expansion and the properties of a second-rank isotropic tensor, a more accurate SPH approximation for the gradient of an arbitrary function can be introduced as

$$\frac{\partial f^p(\vec{\mathbf{r}}_{\mathbf{i}})}{\partial x_{\mathbf{i}}^k} a_{\mathbf{ij}}^{ks} = \sum_{\mathbf{j}=1}^{N} \frac{m_{\mathbf{j}}}{\rho_{\mathbf{j}}} \left(f^p(\vec{\mathbf{r}}_{\mathbf{j}}) - f^p(\vec{\mathbf{r}}_{\mathbf{i}}) \right) \frac{\partial W(r_{\mathbf{ij}},h)}{\partial x_{\mathbf{i}}^s} \tag{8}$$

where $a_{\mathbf{ij}}^{ks} = \sum_{\mathbf{j}=1}^{N} (m_{\mathbf{j}}/\rho_{\mathbf{j}}) r_{\mathbf{ji}}^k \left(\partial W(r_{\mathbf{ij}},h)/\partial x_{\mathbf{i}}^s \right)$ is a corrective second-rank tensor. This form is referred to as corrective SPH gradient formulation that can eliminate particle inconsistency. It should be noted that the corrective term $a_{\mathbf{ij}}^{ks}$ is ideally equal to Kronecker delta δ^{ks} for a continuous function.

In the SPH literature, there are two main forms of the SPH approximation for the Laplacian of a vector-valued function [13, 14].

We have in appendix shown that these two forms can be derived from the SPH form of the second spatial derivative of a vector field $\partial^2 f^p(\vec{\mathbf{r}}_{\mathbf{i}})/\partial x_{\mathbf{i}}^k \partial x_{\mathbf{i}}^l$ as

$$\frac{\partial^2 f^p(\vec{\mathbf{r}}_{\mathbf{i}})}{\partial x_{\mathbf{i}}^k \partial x_{\mathbf{i}}^k} a_{\mathbf{ij}}^{pm} = 8 \sum_{\mathbf{j}=1}^{N} \frac{m_{\mathbf{j}}}{\rho_{\mathbf{j}}} \left(f^p(\vec{\mathbf{r}}_{\mathbf{i}}) - f^p(\vec{\mathbf{r}}_{\mathbf{j}}) \right) \frac{r_{\mathbf{ij}}^p}{r_{\mathbf{ij}}^2} \frac{\partial W(r_{\mathbf{ij}},h)}{\partial x_{\mathbf{i}}^m} \tag{9}$$

$$\frac{\partial^2 f^p(\vec{\mathbf{r}}_{\mathbf{i}})}{\partial x_{\mathbf{i}}^k \partial x_{\mathbf{i}}^k} \left(2 + a_{\mathbf{ij}}^{ll}\right) = 8 \sum_{\mathbf{j}=1}^{N} \frac{m_{\mathbf{j}}}{\rho_{\mathbf{j}}} \left(f^p(\vec{\mathbf{r}}_{\mathbf{i}}) - f^p(\vec{\mathbf{r}}_{\mathbf{j}}) \right) \frac{r_{\mathbf{ij}}^s}{r_{\mathbf{ij}}^2} \frac{\partial W(r_{\mathbf{ij}},h)}{\partial x_{\mathbf{i}}^s} \tag{10}$$

Upon replacing the corrective second rank tensor in Equation (9) and its trace in Equation (10) by the Kronecker delta and its trace, respectively, one can obtain the SPH Laplacian

formulations of a vector-valued function commonly used in SPH literature. Unlike Equation (10), Equation (9) can only be used for divergence free vector- valued functions. Throughout this work, all modelling results are obtained with the usage of corrective SPH discretization schemes, and Equation (9) is used for the Laplacian of velocity, while Equation (10) is used for the Laplacian of pressure in the pressure Poisson equation.

SPH SOLUTION ALGORITHMS

WCSPH

The artificial equation of state used in the WCSPH approach is of the following form,

$$P - P_o = c_{\mathbf{i}}^2 \left(\rho - \rho_o\right) \tag{11}$$

where ρ_o, p_o, c are the reference density (taken as the real fluid density), reference pressure, and the speed of sound. This state equation enforces the incompressibility condition on the flow such that a small variation in density produces a relatively large change in pressure whereby preventing the dilatation of the fluid. The speed of sound $c_{\mathbf{i}}$ for each particle must be chosen carefully to ensure that the fluid is very closely incompressible. The square of the sound speed might be estimated

$$c_{\mathrm{i}}^2 \approx \varphi \; max\left(\frac{v_{\max}^2}{\delta}, \frac{\mu}{\rho_o}\left(\frac{v_{\max}}{L_o \delta}\right), \frac{F^B L_o}{\delta}\right) \tag{12}$$

where φ is problem dependent coefficient, $v_{\max}$ is the maximum value of the fluid velocity, L_o is a characteristic length, F^B is a body force, δ is the relative incompressibility or the density variation factor, which is defined as $\delta = \Delta\rho / \rho_o = v_{\max}^2 / c_{\mathrm{i}}^2 = M^2$, where M is the Mach number. Upon selecting the sound speed much larger than the fluid velocity (at least an order of magnitude) thereby resulting in a very small Mach number, the density variation can be limited to 1% ($\delta \approx 0.01$), which is used this work.

The speed of sound chosen has a direct effect on the permissible time-step in a given simulation. The algorithm stability is controlled by the Courant-Friedrichs-Lewy (CFL) condition, where the recommended time-step [15] is $\Delta t \le C_{CFL} h_{\mathbf{ij},\min} / \left(c_{\mathbf{i}} + v_{\max}\right)$ where $h_{\mathbf{ij}} = 0.5\left(h_{\mathbf{i}} + h_{\mathbf{j}}\right)$, $h_{\mathbf{ij},min}$ is the minimum smoothing length among all **i-j** particle pairs, C_{CFL} is a constant satisfying $0 < C_{CFL} \le 1$ (in this work, $C_{CFL} = 0.125$.)

In order to increment the time-steps in WCSPH algorithm, we have used a predictor corrector method. This technique is an explicit time integration scheme, and is relatively simple to implement. Particle positions, densities, and velocities are computed respectively as

$$D\vec{\mathbf{r}}_{\mathbf{i}} / Dt = \vec{\mathbf{v}}_{\mathbf{i}}, \quad D\rho_{\mathbf{i}} / Dt = k_{\mathbf{i}}, \quad D\vec{\mathbf{v}}_{\mathbf{i}} / Dt = \vec{\mathbf{f}}_{\mathbf{i}} \tag{13}$$

The time integration scheme starts with the predictor step to compute the intermediate particle positions and densities as $\vec{\mathbf{r}}_{\mathbf{i}}^{(n+1/2)} = \vec{\mathbf{r}}_{\mathbf{i}}^{(n)} + 0.5\vec{\mathbf{v}}_{\mathbf{i}}^{(n)}\Delta t$ and $\rho_{\mathbf{i}}^{(n+1/2)} = \rho_{\mathbf{i}}^{(n)} + 0.5k_{\mathbf{i}}^{(n)}\Delta t$ respectively. Having computed the intermediate particle positions and densities during the first half time step, the pressure is computed using Equation (11), while the velocity is computed by $\vec{\mathbf{v}}_{\mathbf{i}}^{(n+1)} = \vec{\mathbf{v}}_{\mathbf{i}}^{(n)} + \vec{\mathbf{f}}_{\mathbf{i}}^{(n+1/2)}\Delta t$. In the next half time (the corrector step), the particle positions and densities are updated as $\vec{\mathbf{r}}_{\mathbf{i}}^{(n+1)} = \vec{\mathbf{r}}_{\mathbf{i}}^{(n+1/2)} + 0.5\vec{\mathbf{v}}_{\mathbf{i}}^{(n+1)}\Delta t$, and $\rho_{\mathbf{i}}^{(n+1)} = \rho_{\mathbf{i}}^{(n+1/2)} + 0.5k_{\mathbf{i}}^{(n+1)}\Delta t$. Note that in order to differentiate between spatial and temporal indices, the time index n is put within brackets.

Instabilities and their possible remedies in SPH method

The homogeneity of the particle distribution is quite important for the accuracy and the robustness of SPH models. Highly irregular particle distributions which may occur as the solution progress may cause numerical algorithms to break down. For instance, if the pressure field is solved correctly thereby imposing the incompressibility condition as accurately as possible, the particle motion closely follow the trajectory of streamline, hence resulting in a linear clustering and in turn fracture in particle distribution. In these regions due to the lack of sufficient number of particles, or inhomogeneous particle distribution, the gradients of field variables cannot be computed reliably. Such a situation leads to spurious fields, especially erroneous pressure values in SPH approach. As the computation progress, the error in computed field variables accumulates whereby blowing-up the simulation.

To prevent the particle clustering, the trajectory of particles can be disturbed by adding relatively small artificial displacement $\delta r_{\mathbf{i}}^k$ to the advection of particles computed by the solution of the equation of motion. Recall the form of a Lennard–Jones potential (LJP)-type force used in the SPH literature as a repulsive force for the solid boundary treatment,

$$F_{\mathbf{i},LJP}^k = \sum_{\mathbf{j}}^{N}\left[\left(r_o / r_{\mathbf{ij}}\right)^{n_1} - \left(r_o / r_{\mathbf{ij}}\right)^{n_2}\right]\frac{\beta r_{\mathbf{ij}}^k v_{\max}^2}{r_{\mathbf{ij}}^2} \tag{14}$$

where $F_{\mathbf{i},LJP}^k$ is the force per unit mass on fluid particle **i** due to the neighbor particles **j**, n_1 and n_2 are constants, β is a problem-dependent parameter, r_o is the cutoff distance at which the inter-particle potential is zero, and $v_{\max}$ is the largest particle velocity in the system. If the second term (attractive interaction) on the right-hand side of LJP force is neglected, and

$n_1 = 2$, and the force $F^k_{\mathbf{i},LJP}$, and $v_{\max}$ are replaced by $\delta r^k_{\mathbf{i}}/(\Delta t)^2$ and $r_{\mathbf{ij}}/\Delta t$, one can write the relationship

$$\delta r^k_{\mathbf{i}} = \beta \sum_{\mathbf{j}}^{N} \frac{r^k_{\mathbf{ij}}}{r^3_{\mathbf{ij}}} r_o^2 v_{\max} \Delta t \tag{15}$$

where $\delta r^k_{\mathbf{i}}$ is an artificial particle displacement vector.

Here, the cut-off distance can be approximated as $r_o = \sum_{\mathbf{j}}^{N} r_{\mathbf{ij}}/N$.

Since the repulsive force depends exponentially on the distance and goes to infinity at $r_{\mathbf{ij}} = 0$, when the distances between two particles decreases, a stronger repulsive force between the closer particles is generated, hence clustering of particles is effectively avoided. Given that $r^k_{\mathbf{ij}} / r^3_{\mathbf{ij}}$ is an odd function with vanishing integral, one can write $\sum_{\mathbf{j}}^{N} r^k_{\mathbf{ij}}/r^3_{\mathbf{ij}} = 0$ for a spherically symmetric particle distribution. However, if the particle distribution is asymmetric, and clustered, the term $\sum_{\mathbf{j}}^{N} r^k_{\mathbf{ij}}/r^3_{\mathbf{ij}} \neq 0$ is no longer equal to zero, whereby implying the region with clustered particle distribution. The artificial particle displacement is only influential in the clustered region and negligibly small in the rest of the computational domain due to $\sum_{\mathbf{j}}^{N} r^k_{\mathbf{ij}} / r^3_{\mathbf{ij}} \cong 0$ provided that the particle distribution is closely uniform.

Boundary condition and domain definition

Mass and linear momentum balance equations are solved for both test cases on a rectangular domain with the length of L=15 m, a height of H =6m. For the first problem a square obstacle with a side dimension of 0.7 m is positioned in the computational domain with its center coordinates at $x=L/3$ and $y=L/2$. Initially, a 349×145 array (in x- and y-directions, respectively) of particles is created in the rectangular domain, and then particles within the square obstacle are removed from the particle array. The boundary particles are created and then distributed on solid boundaries such that their particle spacing is almost the same as initial particle spacing of the fluid particles. The simulation parameters, fluid density, dynamic viscosity and body force are taken as respectively ρ=1000 kg/m^3, μ=1 kg/ms, and F_B^x=3.0x10^{-3} N/kg. Body force per unit mass (F_B^x) is used to model the hydrostatic part of the pressure gradient. The mass of each particle is constant and found through the relation $m_{\mathbf{i}} = \rho_{\mathbf{i}} / n_{\mathbf{i}}$ where $n_{\mathbf{i}} = \sum_{\mathbf{j}=1} W(r_{\mathbf{ij}}, h)$ is the number density of the particle **i**. The smoothing length for all particles is set equal to 1.6 times the initial particle spacing.

The slightly modified periodic boundary condition is implemented for inlet and outlet particles in the direction of the flow. Particles crossing the outflow boundary are reinserted into the flow domain at the inlet from the same y-coordinate positions with the bulk velocity of the fluid so that the inlet velocity profile is not poisoned by the outlet velocity profile. The no-slip boundary condition is implemented for the square obstacle. For upper and lower walls bounding the simulation domain, the symmetry boundary condition for the velocity is applied such that $v^y = 0$, and $\partial v^x / \partial y = 0$ which is discretized by using Equation (8). The no-slip boundary and symmetry boundary conditions are implemented for both test cases using multiple tangent boundary (MBT) method, which is explained in detail in [11].

The channel geometry and the boundary conditions for the second benchmark problem are identical to the first one except that the square obstacle geometry is replaced by the NACA airfoil with a chord length of 2(m) which is created by

$$\begin{aligned} y_c &= m\left(2px_c - x_c^2\right) / p^2 \\ y_c &= m\left(2p(x_c - 1) + 1 - x_c^2\right) / \left(1 - p^2\right) \end{aligned} \qquad \begin{cases} 0 \le x_c \le p \\ p < x_c \le 1 \end{cases} \tag{16}$$

where m is the maximum camber in percentage of the chord, which is taken to be 5%, p is the position of the maximum camber in percentage of the chord that is set to be 50 %, and t is the maximum thickness of the airfoil in percentage of the chord, which is 15 %. The thickness distribution above and below the mean camber line is calculated as

$$\begin{aligned} y_t = 5t(&0.2969 x_c^{0.5} - 0.126 x_c - \\ &0.3516 x_c^2 + 0.284 x_c^3 - 0.1015 x_c^4) \end{aligned} \tag{17}$$

The final coordinates of the airfoil for the upper surface (x_U, y_U) and the lower surface (x_L, y_L) are determined using the following relations: $x_u = x_c - y_t \sin\phi$, $y_U = y_c + y_t \cos\phi$, $x_L = x_c + y_t \sin\phi$, $y_L = y_c - y_t \cos\phi$, and $\phi = \arctan(dy_c/dx)$. Having obtained all coordinates of the airfoil geometry, the upper and lower surface lines are curve fitted using the least square method of order six. In so doing, it becomes possible to compute boundary unit normals, tangents and slopes for each boundary particles. All the initial particles falling between the upper and lower camber fitted curves are removed from the rectangular computational domain, then remaining fluid particles are combined with the boundary particles to form a particle array of the computational domain.

The leading edge of the airfoil is located at Cartesian coordinates (L/5, H/2). Initially, a 300×125 array (in x- and y-directions, respectively) of particles is created in the rectangular domain, and then, particles within the airfoil are removed from the particle array. Subsequently, boundary particles are created

and then distributed on solid boundaries. The smoothing length for all particles is set equal to 1.6 times the initial particle spacing.

FLOW AROUND A SQUARE OBSTACLE AND AN AIRFOIL

In this work, to be able to test the effectiveness of the improved WCSPH algorithm (involving the utility of MBT method together with artificial particle displacement and corrective SPH discretization scheme) for modeling fluid flow over complex geometries, we have solved two benchmark flow problems; namely, two-dimensional simulations of a flow around a square obstacle and NACA airfoil.

The flow around the airfoil and square obstacle positioned inside the channel were simulated for a range of Reynolds numbers $\mathrm{Re}=\rho l_c v_b/\mu$, which is defined by the characteristic length, l_c (set equal to the side length for the square obstacle, and the chord length for the airfoil geometry), the density, the bulk flow velocity v_b and the dynamic viscosity μ. Both test cases are validated through comparing SPH results with those obtained by a Finite Element Method (FEM) based solver of a Comsol multi-physics software tool. The WCSPH and FEM results are compared in terms of velocity contours for both test cases, and the pressure envelope for the airfoil.

Figure 1 compares WCSPH and FEM velocity contours for the Reynolds number value of 100. As can be seen from the figure, the magnitude and the place of contours for the proposed algorithm are in good agreement with those which obtained using FEM in the low Reynolds number range.

It is well-known from both earlier experiments and numerical studies that vortex shedding is observed at the rear edge of the obstacles at higher Reynolds numbers [1, 16, 17]. In light of this, to be able address whether SPH can capture vortex shedding as accurately as mesh dependent solvers, we here present simulation results for Reynolds number of 350. Figures 2 up and down show the simulation results for WCSPH and FEM respectively. It is valuable to mention that in these figures colors show the velocity magnitude. On comparing results, one can notice that results are satisfactorily in agreement with each other regarding the magnitude of velocities as well as the position and number of vortices. However, there is a slight discrepancy between WCSPH and FEM results in terms of the separation point of the vortices from the rear edge of the obstacle. For the sake of brevity, without presenting further results, we can safely assert that SPH method is highly successful in predicting changes of the topology of the vortex shedding behind a square obstacle with the high Reynolds number.

In both test problems solved, the square of the speed of sound is chosen to be equal to ($c^2=25$). Figure 3 reveals that this speed of sound value satisfactorily enforces the fluid incompressibility condition since the density variation is less than 1 percentage.

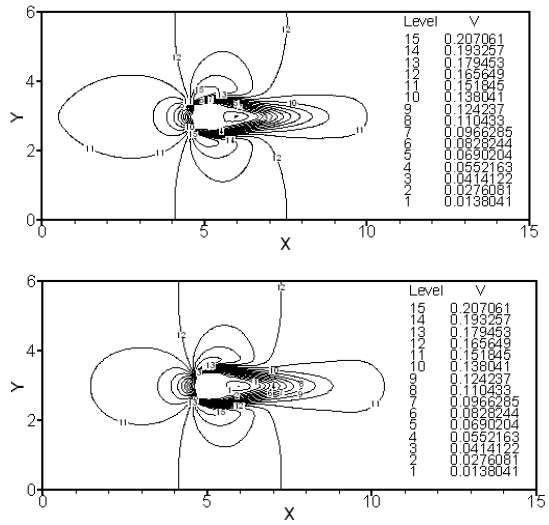

Figure 1: A comparison of WCSPH (up) and FEM (down) velocity contours at Reynolds number 100. It should be noted that in this presentation, all velocities are given as a velocity magnitude

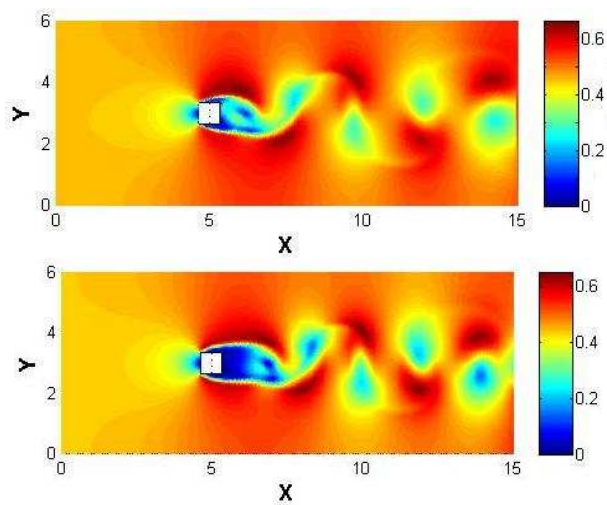

Figure 2: The comparison of vortex shedding contours obtained with WSPH (left) and FEM (right) methods for the Reynolds number of 350 (colors show the velocity magnitude)

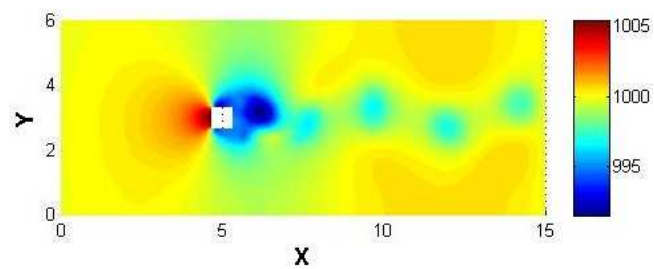

Figure 3: The density contours obtained with WCSPH method for the Reynolds number of 350 (colors show the density values). The utilized speed of sound satisfactorily enforces incompressibility condition.

To have a closer look at the vortex shedding behavior captured at the trailing edge of the square obstacle by WCSPH method,

in Figure 4 are presented the snap shots of vortex shedding for a full period (each snap shot corresponds to one-sixth of the full period) for the Reynolds number of 350.

Figure 5 presents a close-up view of particle positions around airfoils with the angles of attack of 15 degree corresponding to the Reynolds numbers of 570 (up) and 1400 (down) respectively. This figure also illustrates the effectivity of using MBT method to treat difficult geometries which is to our best knowledge not achievable with any other boundary treatment methods proposed for meshless approaches. The proposed algorithm is also very successful in simulating the flow around the airfoil geometry with any geometrical orientations across the flow field. For both low and high Reynolds number values, there are no particle depletions in the domains of interest.

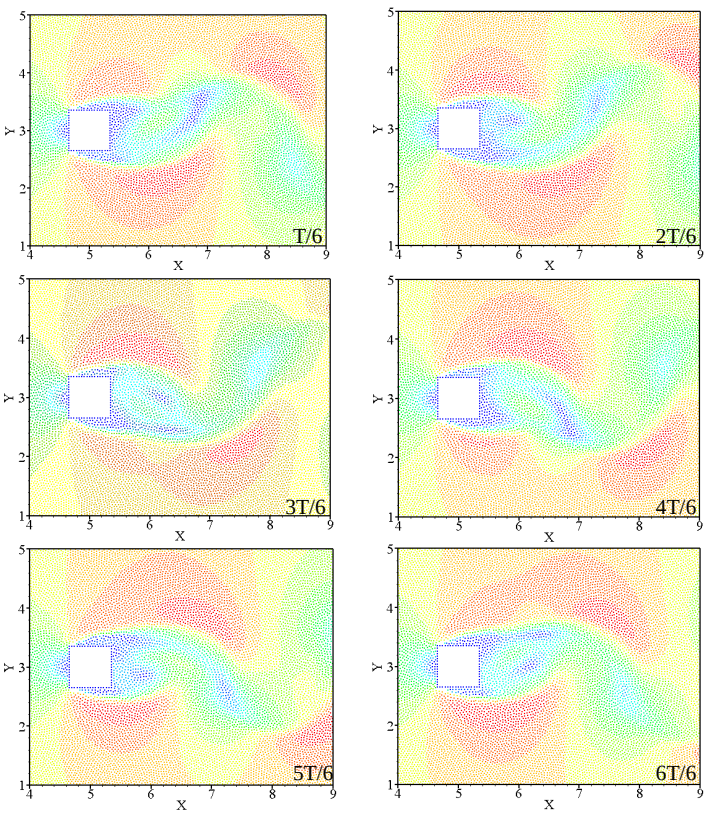

Figure 4: One period of vortex shedding for the square obstacle problem for the Reynolds number of 350 (colors show the velocity magnitude)

It is critical to mention that without the artificial particle displacement algorithm presented and implemented in this work, unphysical particle fractures occur around the airfoil geometry due to the tendency of SPH particles to follow streamline trajectory as illustrated in Figure 6. This brings about erroneous pressure and velocity fields and in turn blow-up of simulations even for relatively small Reynolds numbers and angle of attack values.

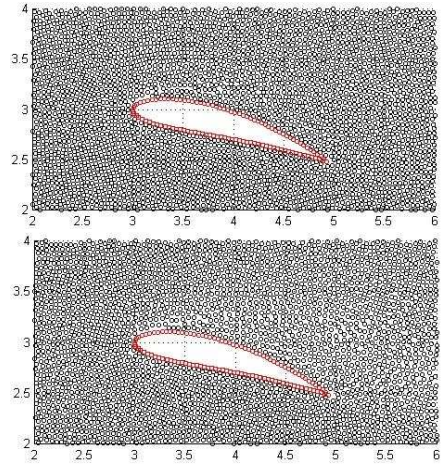

Figure 5: Close-up view of particle positions around airfoils with the angles of attack of 15 degree corresponding to the Reynolds numbers of 570 (up) and 1400 (down)

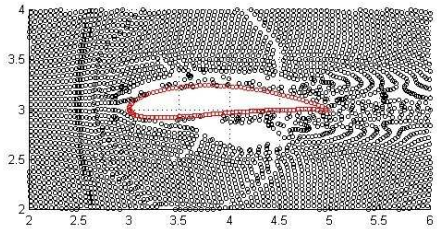

Figure 6: Close-up view of particle positions around the airfoil with the angle of attack of 0 degree corresponding to the Reynolds numbers of 250.

Figure 7 compares SPH and FEM pressure envelopes for the angle of attack of 15 degree with the Reynolds numbers value of 420 (up) and 570 (down). One can rightfully conclude that for both Reynolds number values, WCSPH results are in good agreement with those corresponding to mesh dependent solver. Additionally the pressure differences between upper and lower camber which correlates with the lift force are in match with FEM results for a given position on the boundary.

Figure 8 compares WCSPH and FEM results in terms of the vortex shedding contours for the angle of attack of 5 degree with the Reynolds number of 1400 (colors denote the velocity magnitude). As in the case of the presented square obstacle results, SPH results are also satisfactorily in agreement with FEM regarding the magnitude of velocities as well as the position and number of vortices for the airfoil geometry.

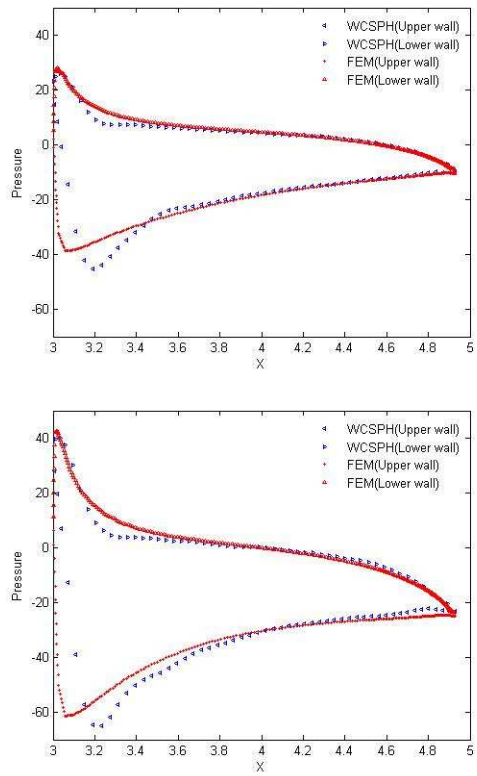

Figure 7: The comparison of pressure envelopes for the angles of attack of 15 for the Reynolds numbers of 420 (up) and 570 (down)

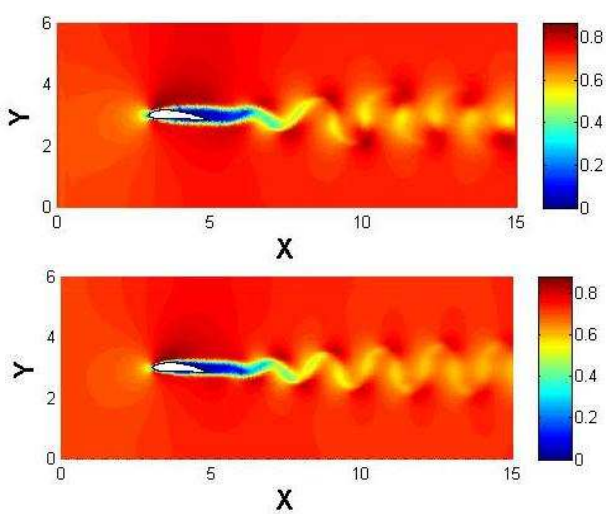

Figure 8: The comparison of vortex shedding contours produced by WCSPH (left) and FEM (right) methods for the angle of attack of 5 degree and the Reynolds number of 1400 (colors show the velocity magnitude)

CONCLUSION

In this work, we present solutions for flow over an airfoil and square obstacle using an improved WCSPH algorithm that can handle complex geometries with the usage of multiple tangent solid boundary method, and eliminate particle clustering induced instabilities with the implementation of artificial particle displacement (particle fracture repair) procedure as well as the corrective SPH discretization scheme. The results were compared in terms of velocity contours for both test cases, and the pressure envelope for the airfoil. Our simulation results were validated with a FEM method, and excellent agreements among the results were observed. We illustrated that the improved WCSPH method is able to capture the complex physics of bluff-body flows naturally such as flow separation, wake formation at the trailing edge, and vortex shedding without any extra effort to increase the particle resolution in some specific areas of interest. We have shown that the improved WCSPH method can be effectively used for flow simulations over bluff-bodies with Reynolds numbers as high as 1400, which is not achievable with standard WCSPH formulations.

ACKNOWLEDGEMENTS

Funding provided by the European Commission Research Directorate General under Marie Curie International Reintegration Grant program with the Grant Agreement number of 231048 (PIRG03-GA-2008-231048) is gratefully acknowledged.

APPENDIX A

The following section provides derivations for the SPH approximation to first- and second-order derivatives of a vector-valued function. The derivations are carried out in Cartesian coordinates. The SPH approximation for the gradient of a vectorial function starts with a Taylor series expansion of $f^p(\vec{\mathbf{r}}_\mathbf{j})$ so that

$$f^p(\vec{\mathbf{r}}_\mathbf{j}) = f^p(\vec{\mathbf{r}}_\mathbf{i}) + r^l_{\mathbf{ji}} \frac{\partial f^p(\vec{\mathbf{r}}_\mathbf{i})}{\partial x^l_\mathbf{i}}\Big|_{\vec{\mathbf{r}}_\mathbf{j}=\vec{\mathbf{r}}_\mathbf{i}} + \frac{1}{2} r^l_{\mathbf{ji}} r^k_{\mathbf{ji}} \frac{\partial f^p(\vec{\mathbf{r}}_\mathbf{i})}{\partial x^l_\mathbf{i} \partial x^k_\mathbf{i}}\Big|_{\vec{\mathbf{r}}_\mathbf{j}=\vec{\mathbf{r}}_\mathbf{i}} \tag{A.1}$$

Upon multiplying Equation (A.1) by the term, $\partial W(r_{\mathbf{ij}},h)/\partial x^s_\mathbf{j}$, and then integrating over the whole space $d^3\vec{\mathbf{r}}_\mathbf{j}$, one can write,

$$\int_\Omega \left(f^p(\vec{\mathbf{r}}_\mathbf{j}) - f^p(\vec{\mathbf{r}}_\mathbf{i})\right) \frac{\partial W(r_{\mathbf{ij}},h)}{\partial x^s_\mathbf{j}} d^3\vec{\mathbf{r}}_\mathbf{j} = \frac{\partial f^p(\vec{\mathbf{r}}_\mathbf{i})}{\partial x^l_\mathbf{i}} \underbrace{\int_\Omega r^l_{\mathbf{ji}} \frac{\partial W(r_{\mathbf{ij}},h)}{\partial x^s_\mathbf{j}} d^3\vec{\mathbf{r}}_\mathbf{j}}_{I^{ls}} + \frac{1}{2} \frac{\partial f^p(\vec{\mathbf{r}}_\mathbf{i})}{\partial x^l_\mathbf{i} \partial x^k_\mathbf{i}} \underbrace{\int_\Omega r^l_{\mathbf{ji}} r^k_{\mathbf{ji}} \frac{\partial W(r_{\mathbf{ij}},h)}{\partial x^s_\mathbf{j}} d^3\vec{\mathbf{r}}_\mathbf{j}}_{I^{lks}=0} \tag{A.2}$$

Note that the first and the second integrals on the right hand side of Equation (A.2) are, respectively, second- and third-rank tensors. The third-rank tensor I^{lks} can be integrated by parts,

which, upon using the Green-Gauss theorem produces Equation (A.3) since the kernel $W\left(r_{\mathbf{ij}},h\right)$ vanishes beyond its support domain.

$$I^{lks}=-\int_{\Omega}W\left(r_{\mathbf{ij}},h\right)\frac{\partial}{\partial r_{\mathbf{j}}^{s}}\left(r_{\mathbf{ji}}^{l}r_{\mathbf{ji}}^{k}\right)d^{3}\vec{\mathbf{r}}_{\mathbf{j}}=-\int_{\Omega}W\left(r_{\mathbf{ij}},h\right)\left(r_{\mathbf{ji}}^{l}\delta^{sk}+r_{\mathbf{ji}}^{k}\delta^{ls}\right)d^{3}\vec{\mathbf{r}}_{\mathbf{j}} \tag{A.3}$$

Recalling that the kernel function is spherically symmetric even function and the multiplication of an even function by an odd function produces an odd function. Integration of an odd function over a symmetric domain leads to zero.

$$I^{lks}=-\delta^{sk}\underbrace{\int_{\Omega}r_{\mathbf{ji}}^{l}W\left(r_{\mathbf{ij}},h\right)d^{3}\vec{\mathbf{r}}_{\mathbf{j}}}_{=0}-\delta^{ls}\underbrace{\int_{\Omega}r_{\mathbf{ji}}^{k}W\left(r_{\mathbf{ij}},h\right)d^{3}\vec{\mathbf{r}}_{\mathbf{j}}}_{=0}=0 \tag{A.4}$$

Following the above described procedure identically, the second rank tensor I^{ls} can be written as

$$I^{ls}=-\delta^{ls}\underbrace{\int_{\Omega}W\left(r_{\mathbf{ij}},h\right)d^{3}\vec{\mathbf{r}}_{\mathbf{j}}}_{=1}=-\delta^{ls} \tag{A.5}$$

On combining Equation (A.2) with Equations (A.4) and (A.5), one can write,

$$\frac{\partial f^{p}\left(\vec{\mathbf{r}}_{\mathbf{i}}\right)}{\partial x_{\mathbf{i}}^{s}}=\int_{\Omega}\left(f^{p}\left(\vec{\mathbf{r}}_{\mathbf{j}}\right)-f^{p}\left(\vec{\mathbf{r}}_{\mathbf{i}}\right)\right)\frac{\partial W\left(r_{\mathbf{ij}},h\right)}{\partial x_{\mathbf{i}}^{s}}d^{3}\vec{\mathbf{r}}_{\mathbf{j}} \tag{A.6}$$

Note that in Equation (A.6), the relationship $\partial W\left(r_{\mathbf{ij}},h\right)/\partial x_{\mathbf{j}}^{s}=-\partial W\left(r_{\mathbf{ij}},h\right)/\partial x_{\mathbf{i}}^{s}$ has been used. Replacing the integration in Equation (A.6) with SPH summation over particle "$\mathbf{j}$" and setting $d^{3}\vec{\mathbf{r}}_{\mathbf{j}}=m_{\mathbf{j}}/\rho_{\mathbf{j}}$, we can obtain the gradient of a vector-valued function in the form of SPH interpolation as.

$$\frac{\partial f^{p}\left(\vec{\mathbf{r}}_{\mathbf{i}}\right)}{\partial x_{\mathbf{i}}^{s}}=\sum_{\mathbf{j}=1}^{N}\frac{m_{\mathbf{j}}}{\rho_{\mathbf{j}}}\left(f^{p}\left(\vec{\mathbf{r}}_{\mathbf{j}}\right)-f^{p}\left(\vec{\mathbf{r}}_{\mathbf{i}}\right)\right)\frac{\partial W\left(r_{\mathbf{ij}},h\right)}{\partial x_{\mathbf{i}}^{s}} \tag{A.7}$$

It is important to note that the second rank tensor I^{ls}, shown to be equal to kronecker delta for a continuous function, may not be equal to kronecker delta for discrete particles. Hence, for the accuracy of the computations, this term should be included in the SPH gradient interpolation of a function. From Equation (A.2), we can write

$$\sum_{\mathbf{j}=1}^{N}\frac{m_{\mathbf{j}}}{\rho_{\mathbf{j}}}\left(f^{p}\left(\vec{\mathbf{r}}_{\mathbf{j}}\right)-f^{p}\left(\vec{\mathbf{r}}_{\mathbf{i}}\right)\right)\frac{\partial W\left(r_{\mathbf{ij}},h\right)}{\partial x_{\mathbf{i}}^{s}}=\frac{\partial f^{p}\left(\vec{\mathbf{r}}_{\mathbf{i}}\right)}{\partial x_{\mathbf{i}}^{l}}\sum_{\mathbf{j}=1}^{N}\frac{m_{\mathbf{j}}}{\rho_{\mathbf{j}}}r_{\mathbf{ji}}^{l}\frac{\partial W\left(r_{\mathbf{ij}},h\right)}{\partial x_{\mathbf{i}}^{s}} \tag{A.8}$$

Equation (A.8) can be written in matrix form as

$$\begin{bmatrix}\sum_{\mathbf{j}=1}^{N}f_{\mathbf{ji}}^{(1)}a_{\mathbf{j}}^{(1)}\\ \sum_{\mathbf{j}=1}^{N}f_{\mathbf{ji}}^{(1)}a_{\mathbf{j}}^{(2)}\end{bmatrix}=\begin{bmatrix}\sum_{\mathbf{j}=1}^{N}r_{\mathbf{ji}}^{(1)}a_{\mathbf{j}}^{(1)} & \sum_{\mathbf{j}=1}^{N}r_{\mathbf{ji}}^{(2)}a_{\mathbf{j}}^{(1)}\\ \sum_{\mathbf{j}=1}^{N}r_{\mathbf{ji}}^{(1)}a_{\mathbf{j}}^{(2)} & \sum_{\mathbf{j}=1}^{N}r_{\mathbf{ji}}^{(2)}a_{\mathbf{j}}^{(2)}\end{bmatrix}\begin{bmatrix}\frac{\partial f_{\mathbf{i}}^{(1)}}{\partial x_{\mathbf{i}}^{(1)}}\\ \frac{\partial f_{\mathbf{i}}^{(1)}}{\partial x_{\mathbf{i}}^{(2)}}\end{bmatrix} \tag{A.9}$$

where $a_{\mathbf{j}}^{s}=\left(m_{\mathbf{j}}/\rho_{\mathbf{j}}\right)\left(\partial W\left(r_{\mathbf{ij}},h\right)/\partial x_{\mathbf{i}}^{s}\right)$.

Starting with the relation for the SPH second-order derivative approximation [11] of a vector valued-function $f^{p}(\vec{\mathbf{r}}_{\mathbf{i}})$ given in Equation (A.10)

$$2\int_{\Omega}\left(f^{p}\left(\vec{\mathbf{r}}_{\mathbf{i}}\right)-f^{p}\left(\vec{\mathbf{r}}_{\mathbf{j}}\right)\right)\frac{r_{\mathbf{ij}}^{s}}{r_{\mathbf{ij}}^{2}}\frac{\partial W\left(r_{\mathbf{ij}},h\right)}{\partial x_{\mathbf{i}}^{m}}d^{3}\vec{\mathbf{r}}_{\mathbf{j}}=\frac{2}{\xi}\frac{\partial^{2}f^{p}\left(\vec{\mathbf{r}}_{\mathbf{i}}\right)}{\partial x_{\mathbf{i}}^{s}\partial x_{\mathbf{i}}^{m}}+\frac{1}{\xi}\frac{\partial^{2}f^{p}\left(\vec{\mathbf{r}}_{\mathbf{i}}\right)}{\partial x_{\mathbf{i}}^{k}\partial x_{\mathbf{i}}^{k}}\delta^{sm} \tag{A.10}$$

which, upon contracting on indices *p* and s, one can obtain

$$2\int_{\Omega}\left(f^{p}\left(\vec{\mathbf{r}}_{\mathbf{i}}\right)-f^{p}\left(\vec{\mathbf{r}}_{\mathbf{j}}\right)\right)\frac{r_{\mathbf{ij}}^{p}}{r_{\mathbf{ij}}^{2}}\frac{\partial W\left(r_{\mathbf{ij}},h\right)}{\partial x_{\mathbf{i}}^{m}}d^{3}\vec{\mathbf{r}}_{\mathbf{j}}=\frac{1}{\xi}\frac{\partial^{2}f^{p}\left(\vec{\mathbf{r}}_{\mathbf{i}}\right)}{\partial x_{\mathbf{i}}^{k}\partial x_{\mathbf{i}}^{k}}\delta^{pm} \tag{A.11}$$

Note that the first term on the right hand side of Equation (A.10) becomes $\partial^{2}f^{p}\left(\vec{\mathbf{r}}_{\mathbf{i}}\right)/\partial x_{\mathbf{i}}^{p}\partial x_{\mathbf{i}}^{m}$ and consequently drops off if the vector-valued function $f^{p}(\vec{\mathbf{r}}_{\mathbf{i}})$ is assumed to be divergence-free velocity field. Here, the coefficient ξ takes the value of 4 and 5 in two and three dimensions, respectively. We have shown in Equations (A.2) and (A.5) that Kronecker delta can be written as,

$$\delta^{pm}=\int_{\Omega}r_{\mathbf{ji}}^{p}\frac{\partial W\left(r_{\mathbf{ij}},h\right)}{\partial x_{\mathbf{i}}^{m}}d^{3}\vec{\mathbf{r}}_{\mathbf{j}} \tag{A.12}$$

Casting Equation (A.12) into Equation (A.11) leads to

$$2\int_{\Omega}\left(f^{p}\left(\vec{\mathbf{r}}_{\mathbf{i}}\right)-f^{p}\left(\vec{\mathbf{r}}_{\mathbf{j}}\right)\right)\frac{r_{\mathbf{ij}}^{p}}{r_{\mathbf{ij}}^{2}}\frac{\partial W\left(r_{\mathbf{ij}},h\right)}{\partial x_{\mathbf{i}}^{m}}d^{3}\vec{\mathbf{r}}_{\mathbf{j}}=\frac{1}{\xi}\frac{\partial^{2}f^{p}\left(\vec{\mathbf{r}}_{\mathbf{i}}\right)}{\partial x_{\mathbf{i}}^{k}\partial x_{\mathbf{i}}^{k}}\int_{\Omega}r_{\mathbf{ji}}^{p}\frac{\partial W\left(r_{\mathbf{ij}},h\right)}{\partial x_{\mathbf{i}}^{m}}d^{3}\vec{\mathbf{r}}_{\mathbf{j}} \tag{A.13}$$

Equation (A.13) can be written in matrix form as

$$\sum_{\mathbf{j}=1}\left(f_{\mathbf{ij}}^{(1)}r_{\mathbf{ij}}^{(1)}+f_{\mathbf{ij}}^{(2)}r_{\mathbf{ij}}^{(2)}\right)\frac{8}{r_{\mathbf{ij}}^{2}}\begin{bmatrix}a_{\mathbf{j}}^{(1)}\\ a_{\mathbf{j}}^{(2)}\end{bmatrix}=\begin{bmatrix}\sum_{\mathbf{j}=1}r_{\mathbf{ji}}^{(1)}a_{\mathbf{j}}^{(1)} & \sum_{\mathbf{j}=1}r_{\mathbf{ji}}^{(2)}a_{\mathbf{j}}^{(1)}\\ \sum_{\mathbf{j}=1}r_{\mathbf{ji}}^{(1)}a_{\mathbf{j}}^{(2)} & \sum_{\mathbf{j}=1}r_{\mathbf{ji}}^{(2)}a_{\mathbf{j}}^{(2)}\end{bmatrix}\begin{bmatrix}\frac{\partial^{2}f_{\mathbf{i}}^{(1)}}{\partial x_{\mathbf{i}}^{k}\partial x_{\mathbf{i}}^{k}}\\ \frac{\partial^{2}f_{\mathbf{i}}^{(2)}}{\partial x_{\mathbf{i}}^{k}\partial x_{\mathbf{i}}^{k}}\end{bmatrix} \tag{A.14}$$

Upon contracting on indices *s* and *m* of Equation (A.10), an alternative form of Laplacian for a vector field can be obtained as

$$8\sum_{\mathbf{j}=1}^{N}\frac{m_{\mathbf{j}}}{\rho_{\mathbf{j}}}\left(f^{p}\left(\vec{\mathbf{r}}_{\mathbf{i}}\right)-f^{p}\left(\vec{\mathbf{r}}_{\mathbf{j}}\right)\right)\frac{r_{\mathbf{ij}}^{s}}{r_{\mathbf{ij}}^{2}}\frac{\partial W\left(r_{\mathbf{ij}},h\right)}{\partial x_{\mathbf{i}}^{s}}=\left(2+\delta^{ss}\right)\frac{\partial^{2}f^{p}\left(\vec{\mathbf{r}}_{\mathbf{i}}\right)}{\partial x_{\mathbf{i}}^{k}\partial x_{\mathbf{i}}^{k}} \tag{A.15}$$

If the trace of the Kronecker delta in Equation (A.15) is replaced by the trace of Equation (A.12), one can obtain an

alternative form of corrective SPH interpolation for a Laplacian.

REFERENCES

[1] R.F. Huanga, B.H. Lina, S.C.Yen, Time-Averaged Topological Flow Patterns and Their Influence on Vortex Shedding of a Square Cylinder in Crossflow at Incidence, Journal of Fluids and Structures (2010) doi:10.1016/j.jfluidstructs.2010.01.003.

[2] A.K. Dhiman, R.P. Chhabra, V. Eswaran, Flow and Heat Transfer Across a Confined Square Cylinder in the Steady Flow Regime: Effect of Peclet Number, International Journal of Heat and Mass Transfer 48 (2005) 4598–4614.

[3] R.A. Gingold, J.J. Monaghan, Smooth Particle Hydrodynamics: theory and application to non spherical stars, Mon. Not. R. Astron. Soc. 181 (1977) 375.

[4] L.B. Lucy, A Numerical Approach to the Testing of the Fission Hypothesis, Astro. J. 82 (1977) 1013.

[5] R.A. Rook, M. Yildiz, S. Dost, Modelling 2D Transient Heat Transfer Using SPH and Implicit time Integration, Journal of Numerical Heat Transfer B 51 (2007) 1–23.

[6] A.M. Tartakovsky, P. Meakin, A Smoothed Particle Hydrodynamics Model for Miscible Flow in Three-Dimensional Fractures and the Two-Dimensional Rayleigh Taylor Instability. J Comput Phys 207(2) (2005) 610-624.

[7] S.M. Hosseini, M.T. Manzari, S.K. Hannani, A Fully Explicit Three-step SPH Algorithm for Simulation of Non-Newtonian Fluid Flow, Journal of Numerical Methods for Heat and Fluid Flow 17 (7) (2007) 715-735.

[8] S. Kulasegaram, J. Bonet, R.W. Lewis, M. Profit, A Variational Formulation Based Contact Algorithm for Rigid Boundaries in Two-Dimensional SPH Applications. Comp. Mech. 33 (2004) 316–325.

[9] R. Issa, E.S. Lee, D. Violeau, D.R. Laurence, Incompressible separated flows simulation with the smoothed particle hydrodynamics gridless method, Int. J. Numer. Methods Fluids 47 (2005) 1101–1106.

[10] E.-S. Lee, C. Moulinec, R. Xu, D. Violeau, D. Laurence, P. Stansby, Comparisons of weakly compressible and truly incompressible algorithms for the SPH meshfree particle method, J. Comput. Phys. 227 (2008) 8417–8436.

[11] M. Yildiz, R.A. Rook, A. Suleman, SPH with the multiple boundary tangent method. Int. J. Numer. Meth. Engng. 77 (10) (2009) 1416–1438.

[12] J.P. Morris, Analysis of smoothed particle hydrodynamics with applications, Ph.D. thesis, Monash University, Melbourne, Australia, 1996.

[13] J.P. Morris, P.J. Fox, Y. Zhu, Modeling Low Reynolds Number Incompressible Flows Using SPH, J. Comput. Phys. 136 (1997) 214–226.

[14] P.W. Cleary, J.J. Monaghan, Conduction Modelling Using Smoothed Particle Hydrodynamics, J. Comput. Phys. 148 (1999) 227–264.

[15] J.J. Monaghan, Smoothed particle hydrodynamics, Reports on Progress in Physics, 68, 1703–59, 2005.

[16] A. Acrivos, D. D. Snowden, A. S. Grove and E. E. Petersen, The steady separated flow past a circular cylinder at large Reynolds number, J. Fluid Mech. 21 (1965) 737-760.

[17] A. Okajima, Strouhal numbers of rectangular cylinders, J. Fluid Mech. 123 (1982) 379-398.